

Assessment of Wavelet-based Separation Algorithms on Turbulent Boundary Layer Trailing-edge Noise Prediction

D.H. Kang* and S. Lee*

Corresponding author: skulee@ucdavis.edu

* Department of Mechanical and Aerospace Engineering,
University of California, Davis, USA.

Abstract: A wavelet-based separation algorithm is evaluated to investigate the mechanism of the noise source generation under turbulent boundary layer flows over an airfoil and its far-field propagation process. Detailed physical interpretations are made by separating the original pressure signal into the coherent and incoherent sources of the pressure and investigating them at particular frequencies using spectral processing and data-driven techniques. For this purpose, large-eddy simulations are conducted to resolve the aerodynamic flow field as well as the near-field acoustic radiation. The Ffowcs-Williams and Hawking acoustic analogy is performed for the far-field acoustic computations. Numerical solutions are validated against available experimental data at a zero angle incidence and the Reynolds numbers of 320,000 and 400,000 for the wall pressure spectrum and far-field acoustics, respectively. It is found that the wavelet-based separation algorithm converges within a few iterations. It is also found that the decomposed coherent component of the pressure is highly influenced by the interaction of turbulent boundary layer flows with the wall, thus maintaining the high energy spectrum up to the frequency of 20 kHz, while the incoherent component is predominant at the frequency of above 20 kHz. The switch of the coherent to the incoherent source of the pressure and the magnitude of each component are shown to be analogous to ones computed from the conventional wavenumber-frequency decomposition. The underlying physics relevant to trailing-edge noise source and its propagation process are discerned by the decomposed pressures: the coherent source of the pressure describes the near-wall coherent turbulence convection as well as the sound propagation due to the edge scattering, and the incoherent source of the pressure accounts for evanescent waves from the hydrodynamic pressures on the wall and the upstream acoustic propagation in the near field.

Keywords: Large-eddy Simulation, Wavelet Transform, Separation Algorithm, Trailing-edge Noise.

1 Introduction

Trailing-edge noise is generated when a turbulent boundary layer flow is scattered at the sharp edge [1], which inevitably takes place for lifting surfaces utilized in many aerospace applications [2, 3, 4, 5, 6]. Due to stringent regulations in noise levels as it closes to living areas, researchers are motivated to focus on unraveling the noise source and its generation mechanism. Trailing-edge noise predictions have been tackled by several computational frameworks [1]. Physics-based acoustic analogies, such as Amiet's theory [7] and Howe's theory [8], in conjunction with empirical wall pressure spectrum models [9, 10] yield fast computations of trailing-edge noise. The serrated trailing-edge noise prediction based on the analytical formulation [11, 12] and their time efficiency in the design cycle to determine important serration parameters for the noise abatement [6, 13] showed the usefulness of the suggested approach. Large-eddy simulation (LES) rapidly grows with increasing scientific computing capabilities in predicting the highly accurate far-field noise and even resolving the flow-induced noise source in the near field as well as the propagation characteristics [14, 15, 16].

In the numerical prediction of trailing-edge noise, the acoustic field is divided into incident and scattered fields [7]. In the low frequency in which the wavelength of sound is relatively larger than the characteristic length, the near-field pressure is mostly dominated by the compact dipole source while the noncompact source is pronounced in mid to high frequency. However, it is challenging to analyze their relative contributions to the far-field acoustics, which resulted in somewhat contradictory conclusions as to the noise reduction mechanism. For example, it was reported that the noise attenuation achieved by serrations results from the destructive interference between the root and tip of serrations [11, 17]. On the contrary, others weighed a decrease in incident wall pressure fluctuations [16].

Shubham *et al.* [18] recently employed a wavenumber-frequency decomposition in conjunction with LES and divided the pressure signal into the hydrodynamic and acoustic components in a Controlled Diffusion (CD) airfoil. It was found that the pressure hump observed at a high frequency and a high Mach number was attributed to the interaction of hydrodynamic and acoustic waves and the acoustic contribution taking place from the leading-edge separation bubble, which was discovered by the wavenumber-frequency decomposition method. However, the drawback of the wavenumber-frequency decomposition lies on prior knowledge of the propagation direction. Furthermore, the resolution in wavenumber for the flow and acoustic propagation is satisfied only if massive probe installations along the propagation direction are provided in the decomposition process.

The present study is motivated by these drawbacks of the wavenumber-frequency decomposition and aims to apply the novel wavelet-based separation technique to the trailing-edge noise analysis. We decompose the original pressure signal into the coherent and incoherent sources of the pressure by using this novel technique. First, the separation algorithm is assessed in terms of the convergence trend and converged threshold criteria. Then, the wavelet-based decomposed pressures are validated against the traditional wavenumber-frequency decomposition. Lastly, the acoustic sources and sound propagation to the far field are investigated by using the spectral processing and data-driven techniques based on the decomposed pressure dataset on the surface and volume domain.

2 Technical Approach

The geometric modelling and the grid generation are performed using GMSH opensource software [19]. Wall-resolved LES is conducted using OpenFOAM opensource CFD code [20]. Then, Ffowcs Williams-Hawking (FW-H) acoustic analogy is computed by PSU-WOPWOP acoustic code [21, 22, 23]. A wavelet transform and separation algorithm proposed by Mancinelli *et al.* [24, 25] coupled with spectral processing and data-driven techniques are applied to the LES dataset. Following subsections summarize each methodology.

2.1 Numerical Method

NACA 0012 airfoil configuration with a blunt trailing edge is used in the present study. Figure 1 (a) and (b) present a three-dimensional airfoil geometry extruded in the spanwise direction and a two-dimensional O-grid with boundary conditions in the computational domain. Here, c is denoted as the chord length of the airfoil. The no-slip boundary condition is imposed on the airfoil wall. The freestream and nonreflecting boundary conditions are applied on the far-field domain to achieve the Riemann invariant and circumvent wave reflections from the far field to the wall, respectively. The periodic boundary condition is applied to both the front and rear surfaces for a three-dimensional simulation. Lastly, the sponge zone is placed to prevent waves from radiating back to the wall. The acoustic damping source term is set with the frequency of 100 kHz and the stencil of 20 in OpenFOAM. In accordance with this, the maximum sound wave of 2 MHz is damped in the numerical domain. Figure 2 (a) and (b) illustrate near-wall structured meshes and grid spacing in wall units in the streamwise and spanwise direction. The stair-strip geometry is placed at $x/c = 0.125$ to forcefully trigger flow transition, which is numerically modelled to compare with experimental measurements of wall pressure spectra [26]. Figure 2 (b) shows that Δx^+ and Δz^+ are maintained less than 20 and 40 near the tripping region, respectively. In addition, the y^+ is less than 0.1 along the airfoil surface. The total number of cells is 90,442,300 with $n_x = 4308$, $n_y = 323$, and $n_z = 65$ in the streamwise, normal, and spanwise directions, respectively, which is satisfactory for the grid requirement of wall-resolved large-eddy simulations [27].

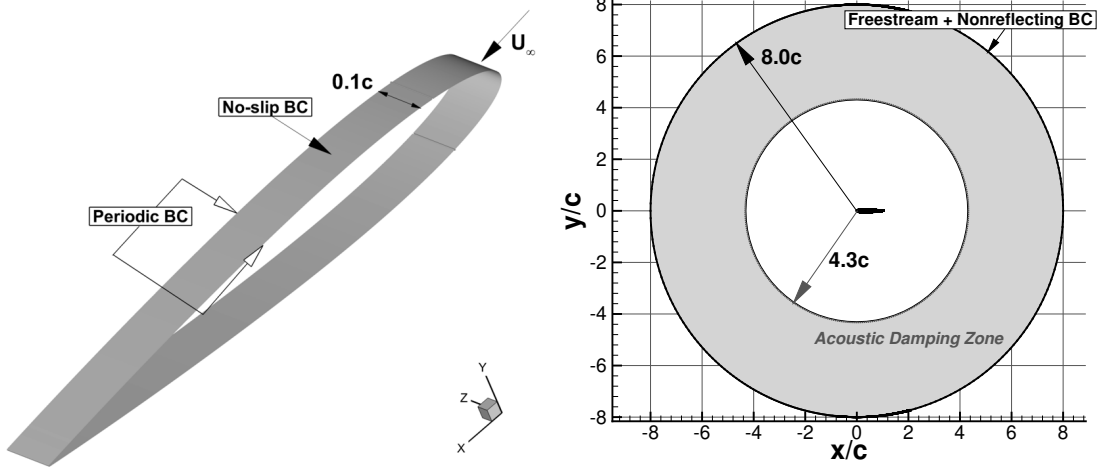


Figure 1: CFD domain: (a) the three-dimensional airfoil surface and (b) the O-type computational domain over the far-field with boundary conditions.

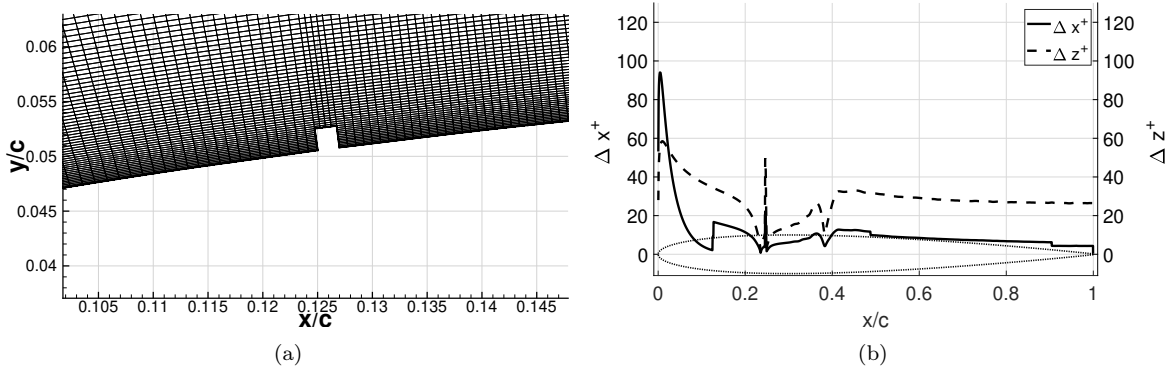


Figure 2: CFD mesh: (a) enlarged near-wall view around the stair-shape tripdot and (b) grid spacing in wall units along the suction side.

Finite volume based rhoPimpleFoam is adopted for the unsteady compressible flow simulation. The Gauss linear scheme is used for the spatial discretization, and the backward-differencing scheme is employed for the temporal discretization. Both numerical schemes have the second order of accuracy. The numerical time step is 10^{-6} s, which corresponds to the maximum CFL number of 0.9. The inner loop iterates every time step until the primitive variables are converged less than 10^{-10} . Wall-adapting local eddy viscosity (WALE) is used as the sub-grid turbulence closure model. The initial condition for LES is computed from the steady-state RANS simulation, which is calculated by the rhoSimpleFOAM solver. Turbulent eddy viscosity is computed using $k-\omega$ SST as a closure model. The total elapsed time in LES equals to 20 airfoil flow-through times (FTT) in which flows reach a statistically convergent state.

2.2 Acoustic Analogy

Acoustic pressure is predicted by using PSU-WOPWOP code [21, 22, 23]. The code numerically solves Farassat's formulation 1A [28, 29], the integral solution of the FW-H equation. Aerodynamic pressure fluctuations extracted on the airfoil surface are utilized to compute the loading noise. The thickness and quadrupole source terms of the FW-H equation are excluded for the low Mach number case. Farassat's formulation 1A for the loading noise is given as follows:

$$p'(\mathbf{x}, t) = p'_L(\mathbf{x}, t) \quad (1)$$

$$\begin{aligned}
4\pi p'_L(\mathbf{x}, t) = & \frac{1}{c} \int_{f=0} \left[\frac{\dot{l}_r}{r|1 - M_r|^2} \right]_{ret} dS + \int_{f=0} \left[\frac{l_r - l_M}{r^2|1 - M_r|^2} \right]_{ret} dS \\
& + \frac{1}{c} \int_{f=0} \left[\frac{l_r(r\dot{M}_r + c(M_r - M^2))}{r^2|1 - M_r|^3} \right]_{ret} dS
\end{aligned} \tag{2}$$

where ρ_∞ is the freestream density, M_r is the airfoil Mach number in the sound radiation direction, $1/|1 - M_r|$ is the Doppler amplification factor, r is a relative distance between the airfoil and an observer, and \dot{l}_r is the rate of change of the surface pressure. The wind tunnel condition where the freestream flow moves toward the airfoil and observers can be converted in the acoustic code such that the airfoil and observers moves in the opposite direction of the freestream velocity in a stationary medium.

2.3 Wavelet-based Separation Algorithm

A pressure signal is decomposed by a discrete wavelet transform. The discrete wavelet coefficients are given by

$$w_p^{(s)}(n) = \sum_{k=-\infty}^{+\infty} \psi^s(n - 2^s k) p(k) \tag{3}$$

where s denotes the discretized scale while the wavelet function $\psi^s(n - 2^s k)$ is the discretized version of $\psi^s = 2^{-\frac{s}{2}} \psi\left(\frac{t}{2^s}\right)$ [30]. A recursive de-noising procedure is used in the present work, which was first applied to vortex dynamics to isolate the coherent vorticity from the incoherent vorticity by Ruppert-Felsot *et al* [31]. Originally, based on statistical reasoning, a threshold developed by Donoho and Johnstone [32] is initially guessed by

$$T_o = \sqrt{2\langle p_{ori}'^2 \rangle \log_2 N_s} \tag{4}$$

where $\langle p_{ori}'^2 \rangle$ is the variance of the original pressure signal and N_s is the number of samples. Starting from the initial guess above, the threshold is updated at each iteration in loop whose formulation can be written as

$$T_k = \sqrt{2\langle p_i'^2 \rangle_k \log_2 N_s} \tag{5}$$

where $\langle p_i'^2 \rangle_k$ indicates the variance of the incoherent source of the pressure signal in time at k_{th} iteration. The flowchart of the separation algorithm is presented in Fig. 3. The incoherent source of the pressure is iteratively decomposed until the number of incoherent wavelet coefficients at the next step is the same as that of the present step. Such a decomposition algorithm is carried out in MATLAB.

2.4 Dynamic Mode Decomposition

Dynamic Mode Decomposition (DMD) is a data-driven method also known as a model based approach, capable of extracting spatiotemporal coherent patterns from the complex system [33]. It was introduced in fluid dynamics by Schmid [34], providing physical insights from high-dimensional flow data. As the inherent nature of DMD is based in both the principal component analysis in space and the Fourier transform in time, the dominant coherent structure at particular frequencies can be explored separately. Pressure data on the suction side of the airfoil is used for DMD analysis. The time-resolved snapshots of the pressure field are collected as n by m matrix, \mathbf{X} .

$$\begin{bmatrix}
| & | & & | \\
\mathbf{x}_1 & \mathbf{x}_2 & \dots & \mathbf{x}_m \\
| & | & & |
\end{bmatrix} \tag{6}$$

Here, n is the number of spatial points saved per time snapshot and m is the number of snapshots taken. With two dynamical sets of data comprised of \mathbf{x}_1 to \mathbf{x}_{m-1} and \mathbf{x}_2 to \mathbf{x}_m , denoted as \mathbf{X}_1 and \mathbf{X}_2 , respectively,

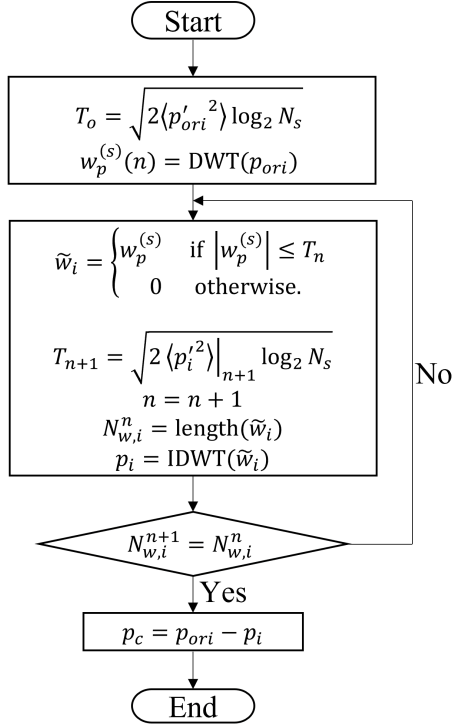


Figure 3: Flowchart of the wavelet-based separation algorithm.

the discrete linear dynamical system is given in the following form:

$$\mathbf{X}_2 \approx \mathbf{A}\mathbf{X}_1 \quad (7)$$

where \mathbf{A} is called a best fit linear operator obtained by minimizing the Frobenius norm of the equation $\|\mathbf{X}_2 - \mathbf{A}\mathbf{X}_1\|_F$. Singular value decomposition (SVD) and eigendecomposition are applied to the matrix, \mathbf{A} , consequently so as to calculate the eigenvalues and eigenvectors. Further details of DMD algorithm are referred in Ref. [33]. The discrete-time DMD eigenvalues are $\lambda_k = \text{Re}(\lambda_k) + \text{Im}(\lambda_k)i$, also called Ritz values. The growth rate is evaluated by its magnitude such that the mode grows if $|\lambda_k| > 1$ and decays otherwise. The continuous-time DMD eigenvalues that represent the stability of eigenmodes are obtained after logarithmic mapping as follows:

$$u_k = \frac{\ln(\lambda_k)}{\Delta t} = \sigma_k + \omega_k i \quad (8)$$

where σ_k represents the growth rate of u_k , and ω_k is the angular frequency of the k_{th} DMD mode. The frequency of the k_{th} DMD mode is defined as $f_k = \omega_k/(2\pi)$. The reconstruction of the pressure field $p(t)$ is expressed as a linear combination of the eigenvectors of the \mathbf{A} matrix (Φ), or the DMD modes, as follows:

$$p(t) \approx \sum_{k=1}^{r-1} \Phi_k \exp(\omega_k t) b_k = \Phi \exp(\Omega t) \mathbf{b} \quad (9)$$

where b_k is the initial amplitude of each DMD mode. Data matrices of the pressure on the suction side of the airfoil are collected at 33,800 probes on the surface of x/c from the leading edge to the trailing edge and z/c from 0 to $0.1c$. The target rank of SVD is set to be 301. A total $N=300$ snapshots are stored from the last FTT, and the sampling rate is 200 kHz ($f = 1/(5dt)$).

3 Results and Discussion

3.1 Validations for Flow and Acoustic Solvers

As pressure fluctuations are the main input to the wavelet analysis, LES dataset is validated against available experimental data including wall pressure spectra [26] and far-field acoustic pressure spectra [35].

Figure 4 illustrates the predictions and experiments of the wall pressure spectra measured at three different streamwise locations: $x/c=0.83, 0.97,$ and 0.99 . The predictions follow the line of f^{-5} behavior [36] related to the wall pressure sources in the buffer layer at beyond 4 kHz of the frequency albeit predictions deviated from experiments at $x/c=0.83$. It is found that excellent agreement is shown at $x/c=0.97$ and 0.99 near the trailing edge though. Figure 5 presents the predicted far-field acoustic pressure spectrum as well as untripped and tripped experiments measured at an observer position of $x = c, y = 8.0c,$ and $z=\text{midspan}$. The tonal peak around 600 Hz is attributed to the modelling effect of the geometrically resolved stair-strip positioned at the 20 percent of the chord. The predicted sound pressure spectrum between 1 and 2 kHz approximates the untripped experiment because of the delay of laminar-to-turbulent transition despite the presence of the boundary-layer forced tripping. Beyond 2 kHz, the broadband shape and its extent are in fairly good agreement with the tripped experiment.

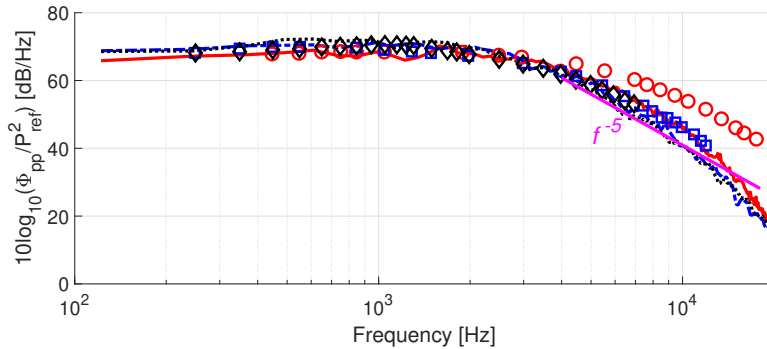


Figure 4: Wall pressure spectra referenced to $p_{ref} = 20\mu Pa$ on the suction side of the airfoil at various streamwise locations. Predictions ($x/c = 0.83$) —, ($x/c = 0.97$) —, and ($x/c = 0.99$) —, and experiments \circ ($x/c = 0.83$), \square ($x/c = 0.97$), and \diamond ($x/c = 0.99$).

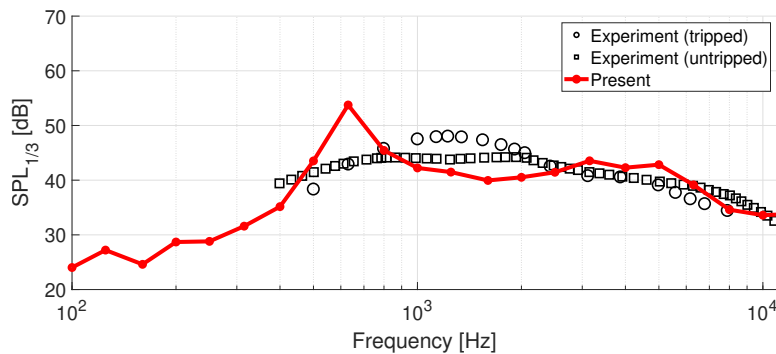


Figure 5: Predicted far-field acoustic pressure spectrum at an observer location of $x = c, y = 8.0c,$ and $z=\text{midspan}$ compared with untripped and tripped experiments.

Instantaneous flow and acoustic events are illustrated in Fig. 6. It is shown that turbulent convection develops after the transition-to-turbulence process, and thereby incident hydrodynamic waves are radiated across the wall. Note that the two-dimensional Tollmien-Schlichting wave (T-S waves) are described by the surface pressure dilatation during flow transition. There are two distinct acoustic perturbations: one is originated from the tripping region, which generates an extraneous tonal peak observed in Fig. 5, whereas

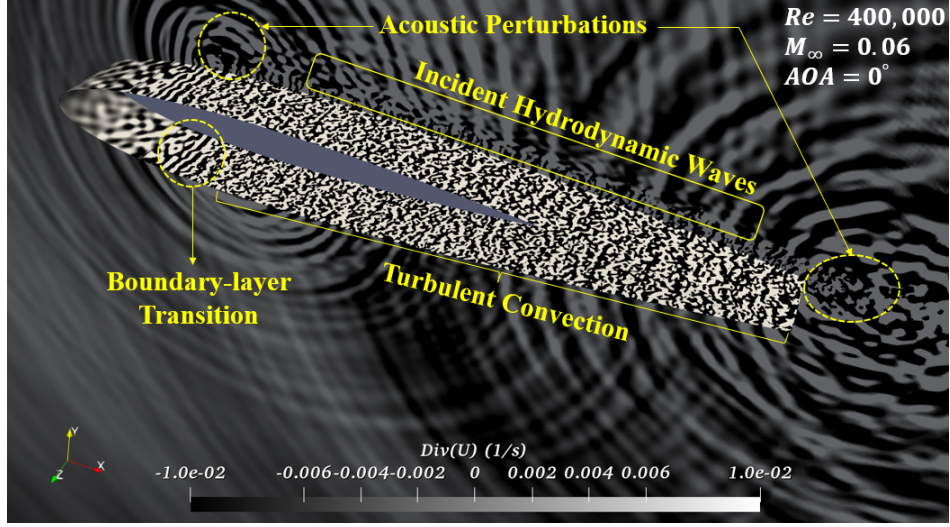


Figure 6: Dilatation field of flow and acoustic events around the airfoil.

the other is in the vicinity of the trailing edge as a result of the edge scattering of turbulent boundary layer flows.

3.2 Assessment of Wavelet-based Separation Algorithm

In this section, the wavelet-based separation algorithm is applied to the pressure field on the suction side of the airfoil and volume domain. First, the evaluation of the convergence trend for the wavelet-based separation algorithm is performed at a single point near the trailing edge. Then, the decomposition process is extended to the entire domain including the airfoil surface and the volume domain around the airfoil, and it is assessed through the converged threshold contour levels. Lastly, the wall pressure spectra of the decomposed pressures as well as the original pressure near the trailing edge are compared with those obtained from the traditional wavenumber-frequency decomposition method for validation purpose.

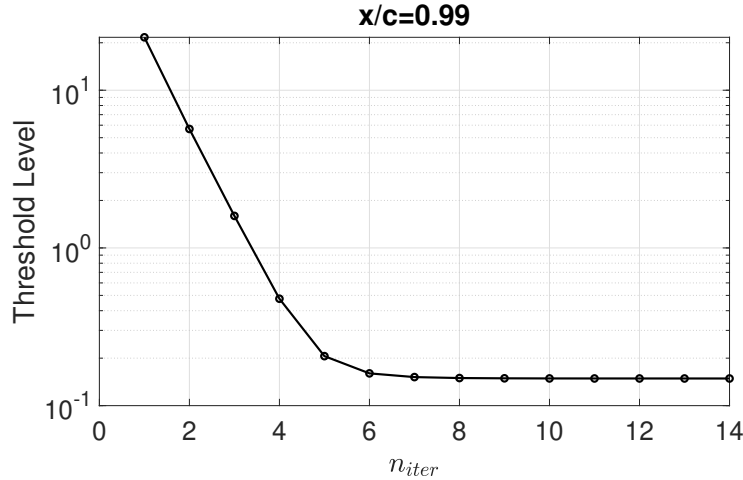


Figure 7: Convergence trend of the threshold level along the iteration on the suction side of the airfoil at $x/c = 0.99$.

The converged threshold value in the separation algorithm designates when the decomposed incoherent source of the pressure reaches the statistically convergent state indicating the constant amplitude in pressure

fluctuations. Thus, the magnitude of the threshold level is proportional to the amplitude of the incoherent source of the pressure. Figure 7 shows the convergence history of the threshold level. It is observed that the threshold level reaches constant after 6 iterations. This convergence trend is accomplished for all probes considered in the present study. Figure 8 illustrates the converged threshold contour levels on the suction of the airfoil. It is seen that the threshold level is nearly zero in the proximity of the leading edge where the flow is premature to enter the stage of turbulent regimes. It means that the original pressure is interpreted as the coherent source of the pressure. On the other hand, the high strength in the threshold value manifests after the onset of flow transition at the 20 percent of the chord length where the incoherent source of the pressure is produced due to the perturbed turbulent flows, i.e., injection of energy. This is clarified by Fig. 9 indicating the quantitative variation of the threshold value along the streamwise direction. In the meantime, the threshold decreases after the production of turbulent flows due to dissipating turbulent eddies.

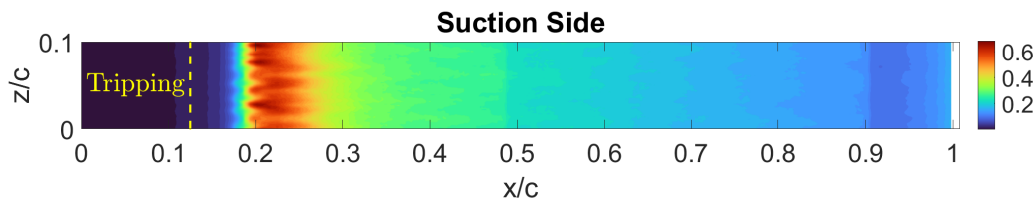


Figure 8: Converged threshold contour levels on the suction side of the airfoil.

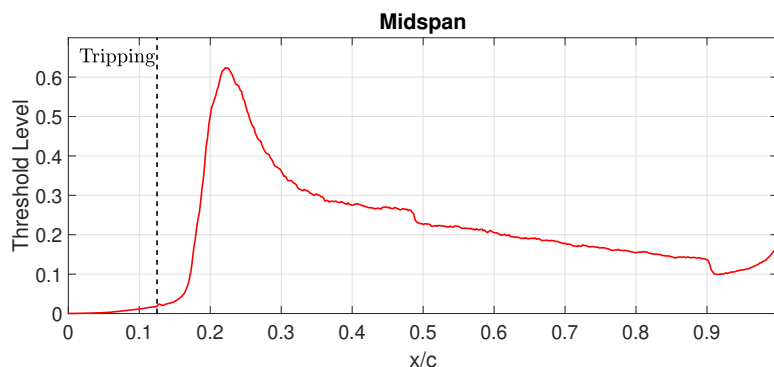


Figure 9: Converged threshold levels on the suction side of the airfoil at midspan.

Figure 10 depicts the spatial contours of the converged threshold level. As in the case of surface distributions of the threshold in Figs. 8 and 9, the local high strength of the threshold is observed near the boundary-layer tripping and wake regions downstream of the trailing edge. These are as a result of the trip-dot-induced perturbation near the leading edge and scattered pressure near the trailing edge, respectively. This will be further discussed in linkage with the dilatation fields of the incoherent source of the pressure. Note that the local high threshold partially smears into the trailing edge, leading to the mild increase in the surface threshold level as depicted in Figs. 8 and 9.

Figure 11 displays the decomposed wall pressure spectra of the coherent and incoherent sources as well as the original one on the suction side of the airfoil at $x/c = 0.99$. One can observe that the high energy spectrum is occupied by the coherent source of the pressure at low-to-mid frequencies while the high frequency spectrum is dominated by the incoherent source of the pressure. The high energy spectrum of the coherent source of the pressure is associated with the intermittent behavior of turbulent flows and their interaction with the wall. The results contrast to the observation in high-speed jet flows where the magnitude of the incoherent pressure spectra is higher than the present case and the switch from the coherent to incoherent pressure occurs at lower frequencies [37, 25]. It is speculated that the difference results from the presence of the wall and the low Mach number regimes in the present case.

Figure 12 depicts the wavenumber-frequency spectrum calculated from surface probes from $0.49c$ to $0.99c$.

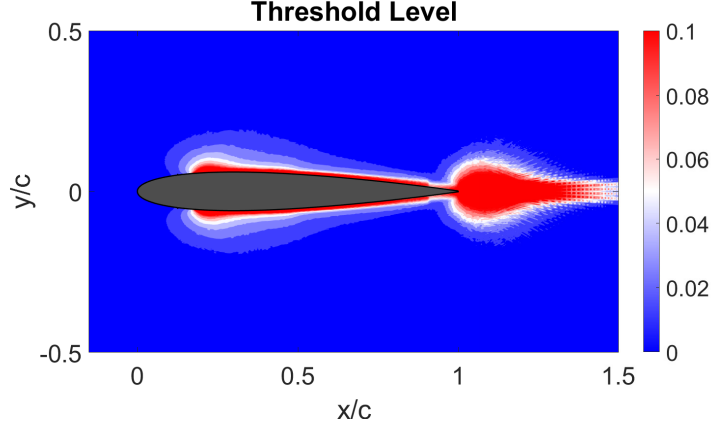


Figure 10: Converged threshold contour levels on the space cut at midspan.

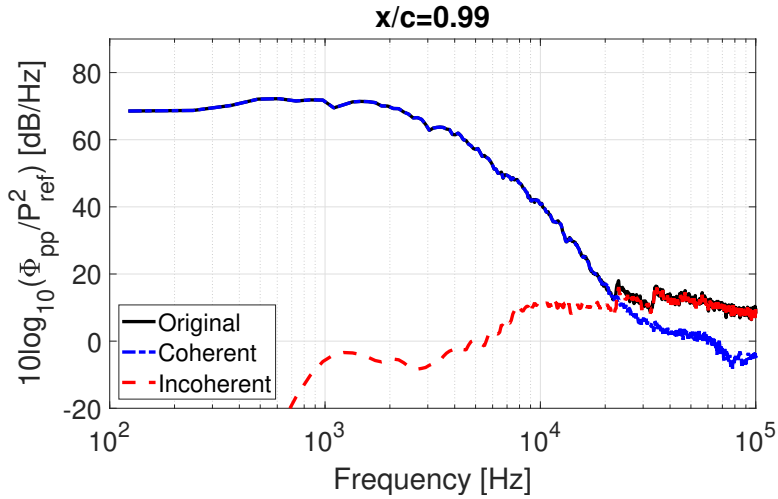


Figure 11: Wall pressure spectra of the coherent, and incoherent sources of the pressure decomposed by the wavelet-based separation algorithm as well as the original pressure at $x/c = 0.99$.

256 probes are uniformly placed to give a wavenumber resolution of $\Delta k = 6.77 m^{-1}$ defined as $\Delta k = 1/(Ndx)$. It is shown that the positive wide-band ridge has the high spectral level associated with turbulent flows with a convection speed denoted as U_c . Note that the upstream acoustic propagation is confirmed by $U_c - c$ line where c is the speed of sound. Three phase speeds including the hydrodynamic turbulent convection and the upstream/downstream acoustic propagation can also be decomposed by the wavenumber-frequency decomposition. The decomposition procedure through the wavenumber-frequency spectrum is described in detail in Refs. [18, 38]. Figure 13 presents three decomposed pressures in addition to the original pressure at $x/c = 0.99$. It is found that the high spectral level is represented by the hydrodynamic pressure while the acoustic source of the pressure accounts for the high-frequency energy spectrum, which is analogous to the results of wavelet-based separation. It is also found that the switch of the contribution from the hydrodynamic to the acoustic pressure occurs near the frequency of 20 kHz, which agrees with the result obtained from the wavelet-based decomposition. Hence, it demonstrates that the wavelet-based separation algorithm produces the consistent solutions with the traditional wavenumber-frequency decomposition in the problem of wall-bounded flows. In sum, when restricted to the wall pressure, the coherent pressure is referred to as the hydrodynamic pressure whereas the incoherent pressure is thought as the acoustic pressure. The upstream acoustic propagation based on the incoherent pressure will be further discussed in the DMD analysis.

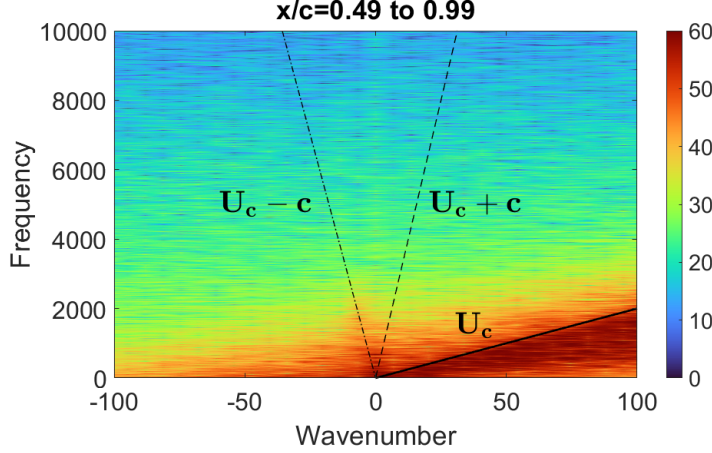


Figure 12: Wavenumber-frequency spectrum on the suction side of the airfoil from $x/c = 0.49$ to 0.99 .

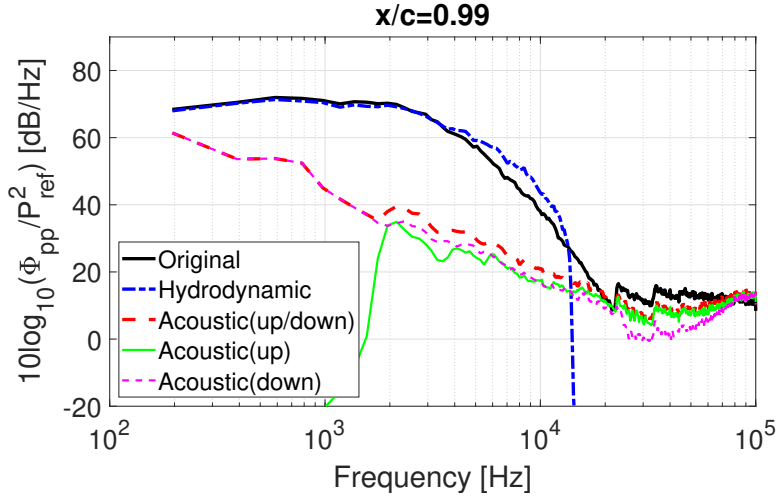


Figure 13: Wall pressure spectra of the original pressure, the hydrodynamic, and the acoustic pressures obtained from wavenumber-frequency decomposition at $x/c = 0.99$.

3.3 Spatial Distributions of Decomposed Pressures near Wall and Far Field

The usefulness of the wavelet-based separation is in the simplicity to the required setup [25]. It indeed requires only one probe of interest in the surface or space, which implies that a prior knowledge of the propagation direction is not needed. When the advantage of the wavelet-based separation algorithm is combined with the flexibility of numerical simulations capable of placing the virtual probes in the volume domain without any restriction, it enables to explore underlying physical mechanism of the origin of the noise source in the near wall and its propagation to the far field. Hence, the coherence level, dilatation fields, and dynamic mode decomposition are employed and coupled with the wavelet-based decomposition in this section.

The space-surface pressure coherence is defined as follows:

$$\gamma_{p_s p_w}^2 = \frac{|S_{p_s p_w}|^2}{|S_{p_s p_s}| |S_{p_w p_w}|} \quad (10)$$

where S stands for either a cross-power spectral density if two statistical quantities are different or an auto-power spectral density otherwise. p_s is the pressure on the space: for example, the near-wall or the far-field while p_w is the wall pressure. Here, p_s is fixed as the original pressure when calculating the coherence but

p_w is repeatedly replaced with the original pressure and two decomposed pressures. Figure 14 shows the space-surface pressure coherence on the suction side of the airfoil at $x/c = 0.99$. It is evident that the coherent source of the pressure is highly correlated with the pressure on the space at low-to-mid frequencies within the inner layer, which is the main mechanism of the coherent noise source generation. However, the high level of the incoherent source of the pressure is stretched from wall to outer layer, which is ascribed to the edge scattering. The high-frequency dominance of the incoherent source of the pressure is consistent with the behavior on the wall, as observed in Fig. 11.

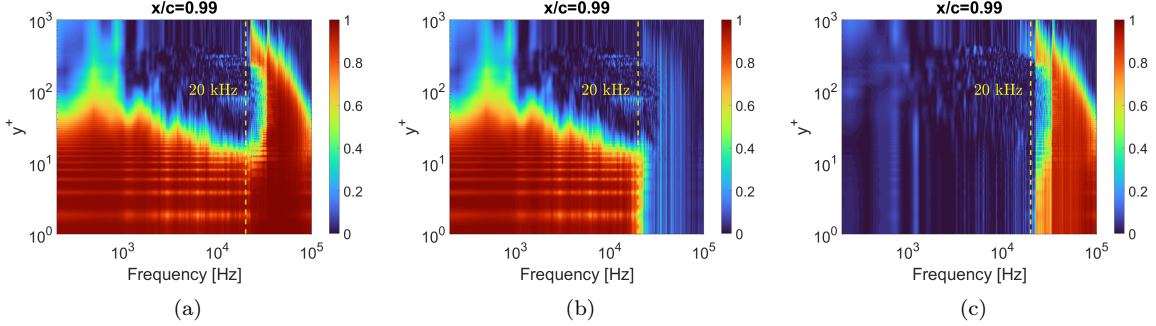


Figure 14: $\gamma_{p_s p_w}^2$ of the original pressure (a), the coherent (b) and incoherent (c) sources of the pressure at $x/c = 0.99$.

According to Mancinelli *et al.* [25], the sound pressure spectrum level (SPSL) is calculated as follows:

$$\text{SPSL} = 10 \log_{10} \frac{\text{PSD} \Delta f_{ref}}{p_{ref}^2} \quad (11)$$

where PSD is the power spectral density of the pressure, $\Delta f_{ref} = 6.66\text{Hz}$, and $p_{ref} = 20\mu\text{Pa}$. SPSLs for the two decomposed pressures as well as the original pressures are plotted in Fig. 16. As in the case of the coherence level, the decomposed coherent pressure maintains the high sound level within the turbulent boundary layer flows up to the the frequency of 20 kHz, however, the incoherent source of the pressure is distinct beyond the frequency of 20 kHz though it has smaller magnitudes in the spectral level.

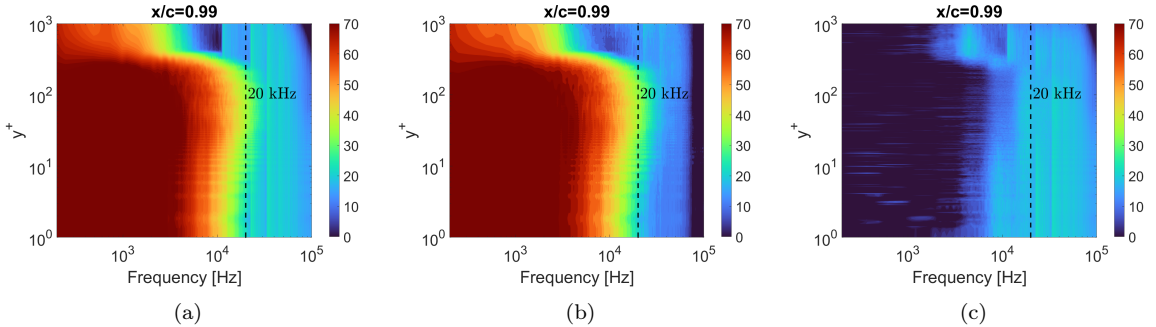


Figure 15: SPSLs of the original pressure (a), the coherent (b), and the incoherent (c) sources of the pressure at $x/c = 0.99$.

Figure 16 illustrates the dilatation fields of the coherent and incoherent sources of the pressure. It is observed that typical coherent turbulent flows near the wall and far-field acoustic propagation by the edge scattering are filtered into the coherent pressure. This means that the coherent pressure in wall-bounded flows involves not only the high-energy spectral turbulence convection but also its propagation mechanism. However, the acoustic perturbation at the tripping region is not clearly captured because it is irrelevant to the hydrodynamic turbulent fluctuations. Meanwhile, the noise cancellation of multiple waves emanated from hydrodynamic incident waves are observed from the incoherent source of the pressure field. This is caused

by the out-of-phase characteristics of the convecting coherent turbulent flows, resulting in evanescent waves, or referred as ‘pseudo sound’ component. It means that the noise emissions from the turbulent convection does not propagate to the far field. The edge scattering mechanism only produces far-field noise unless we consider extraneous noise from the tripping effect. Moreover, the similarity between the spatial pattern of the incoherent source of the pressure (Fig. 16 (b)) and converged threshold contours is confirmed in the dilatation field (Fig. 10).

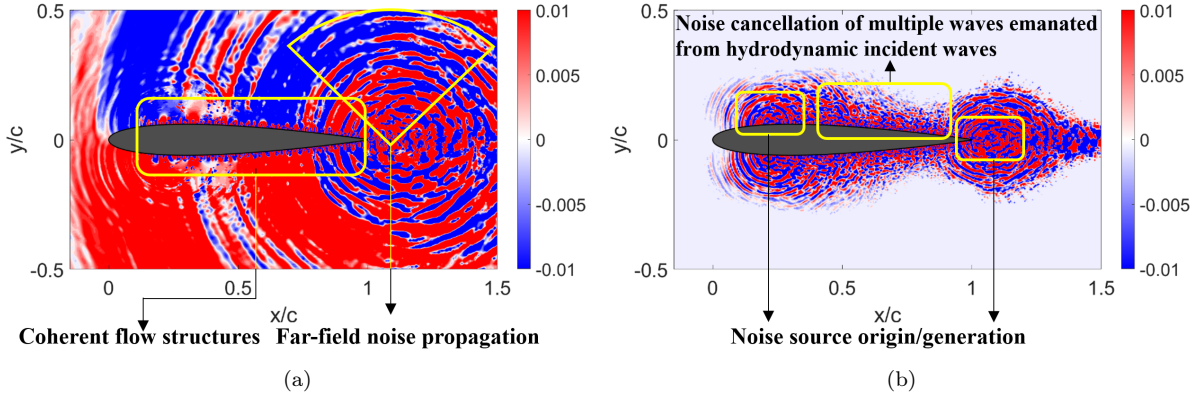


Figure 16: Dilatation fields for the coherent (a) and the incoherent (b) sources of the pressure.

A spatiotemporal coherent flow structure on the suction side of the airfoil is extracted at four different frequencies using DMD. Figure 17 presents DMD modes of the two decomposed pressures from low to high frequencies. In Fig. 17 (a), it is found that the sources of the incident hydrodynamic waves on the wall are in the form of a spanwise coherent but out-of-phase coherent structure in the streamwise direction at 1 and 4 kHz after the onset of the boundary-layer transition process. On the other hand, it is shown in the decomposed incoherent pressure that the upstream acoustic propagation close to the trailing edge is the leading mechanism at 15 and 24 kHz, which was also observed in the wavenumber-frequency spectrum in Figs. 12 and 13. This implies that the wavelet-based separation algorithm is able to capture the multi-dimensional propagation direction though it uses pressure information measured only at one probe. To sum up from the dilatation and DMD contours, the coherent turbulent structure and far-field acoustic propagation are represented by the coherent source of the pressure whereas the origin of noise sources, the noise cancellation of the incident pressures, i.e., evanescent waves, and the upstream propagation mechanism can be identified from the incoherent source of the pressure.

4 Conclusions

A novel wavelet-based separation algorithm has been applied to the trailing-edge noise study. First, the pressure database obtained from the wall-resolved large-eddy simulation was validated against available experimental data showing good agreements in the wall pressure spectra and far-field sound.

It was found that the proposed algorithm converges with a few iterations in the problem of wall-bounded flows. For the converged threshold on the airfoil wall, the local high strength was associated with the trip-induced perturbations near the leading edge and the scattering effect in the proximity of the trailing edge. The decomposed coherent source of the pressure was highly influenced by the turbulence convection and its interaction with the wall, resulting in the high energy spectrum up to 20 kHz of the frequency while the incoherent source of the pressure was responsible for the upstream acoustic program at higher frequencies. The latter was confirmed by the acoustic pressure decomposed from the conventional wavenumber-frequency spectrum. The switch from the coherent to incoherent pressure in the wavelet-based separation method was also found to be analogous to ones calculated from the traditional-wavenumber frequency decomposition.

It was discovered that the coherent wall pressure near the trailing edge has a high correlation with the turbulent boundary layer flow within the inner layer, which is the main mechanism of the coherent

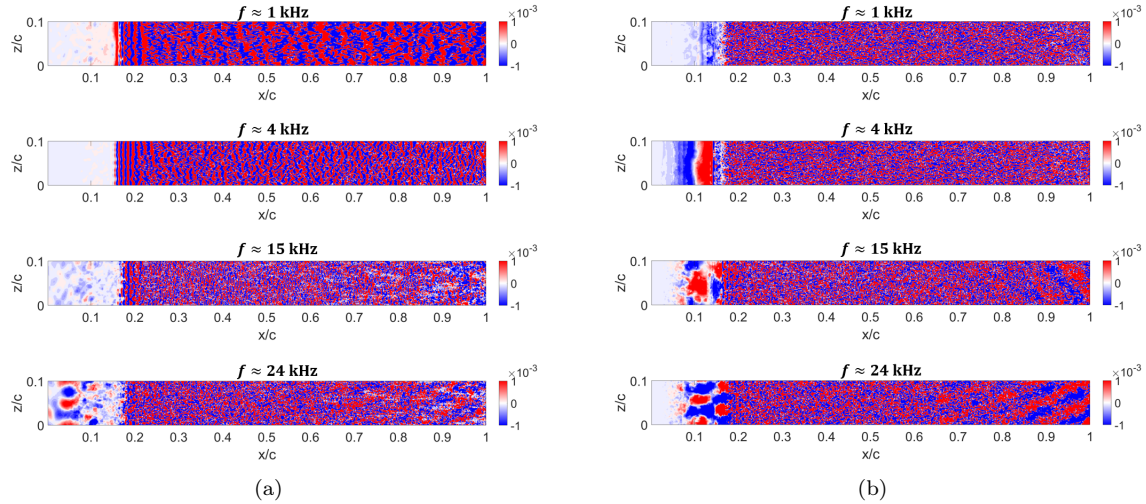


Figure 17: DMD modes on the suction side of the airfoil for the coherent (a) and the incoherent (b) sources of the pressure.

hydrodynamic pressure fluctuations. On the other hand, the incoherent wall pressure was stretched from the wall. The magnitude of the noise source measured by SPSL clarified that the decomposed coherent pressure has the high sound level while the magnitude of the incoherent source of the pressure was relatively smaller than the coherent pressure. It was observed in the dilatation field that the coherent source of the pressure represents the near-wall coherent turbulent structure as well as the far-field sound propagation while the origin of noise source near the wall is captured by the incoherent source of the pressure. The hydrodynamic incident waves emanated from the wall became evanescent waves due to the out-of-phase waves generated along the coherent near-wall turbulence structure. These evanescent waves were captured in the incoherent pressure. It was found from DMD plots that such a coherent structure is prominent at frequencies of 1 and 4 kHz. At high frequencies of 15 and 24 kHz, the upstream acoustic propagation was the leading mechanism, which was captured close to the trailing edge in the incoherent source of the pressure.

References

- [1] S. Lee, L. Ayton, F. Bertagnolio, S. Moreau, T.P. Chong, and P. Joseph. Turbulent boundary layer trailing-edge noise: theory, computation, experiment, and application. *Progress in Aerospace Sciences*, 126:100737, 2021.
- [2] W. Johnson and C. Silva. Nasa concept vehicles and the engineering of advanced air mobility aircraft. *The Aeronautical Journal*, pages 1–33, 2021.
- [3] Z. Jia and S. Lee. Computational study on noise of urban air mobility quadrotor aircraft. *Journal of the American Helicopter Society*, 67:012009, 2022.
- [4] Z. Jia and S. Lee. High-fidelity computational analysis on the noise of a side-by-side hybrid vtol aircraft. *Journal of the American Helicopter Society*, 67:022005, 2022.
- [5] S. Li and S. Lee. Prediction of urban air mobility multi-rotor vtol broadband noise using ucd-quietfly. *Journal of the American Helicopter Society*, 66:032004, 2021.
- [6] S. Li and S. Lee. Acoustic analysis and annoyance assessment of a quiet helicopter for a air taxi operations. *Journal of the American Helicopter Society*, accepted for publication, 2022.
- [7] R. K. Amiet. Noise due to turbulent flow past a trailing edge. *Journal of Sound and Vibration*, 47:387–393, 1976.
- [8] M. S. Howe. *Acoustics of fluid-structure interactions*. Cambridge University Press, 1998.
- [9] S. Lee. Empirical wall-pressure spectral modeling for zero and adverse pressure gradient flows. *AIAA Journal*, 56(5):1818–1829, 2018.

- [10] S. Lee and J. G. Shum. Prediction of airfoil trailing edge noise using empirical wall pressure spectrum models. *AIAA Journal*, 57(3):888–897, 2019.
- [11] L. J. Ayton. Analytic solution for aerodynamic noise generated by plates with spanwise-varying trailing edges. *J. Fluid Mech.*, 849:448–466, 2018.
- [12] B. Lyu and L. J. Ayton. Rapid noise prediction models for serrated leading and trailing edges. *Journal of Sound and Vibration*, 469:115136, 2020.
- [13] S. Li and S. Lee. Extensions and applications of lyu and ayton’s serrated trailing-edge noise model to rotorcraft. In *2022 AIAA/CEAS Aeroacoustics Conference*, Southampton, United Kingdom, June 14–17 2022.
- [14] W. R. Wolf, J. L. Azevedo, and S. K. Lele. Convective effects and the role of quadrupole sources for aerofoil aeroacoustics. *Journal of Fluid Mechanics*, 708:502–538, 2012.
- [15] A. Bodling and A. Sharma. Numerical investigation of noise reduction mechanisms in a bio-inspired airfoil. *Journal of Sound and Vibration*, 453:314–327, 2019.
- [16] M. B. Gelot and J. W. Kim. Broadband noise prediction for aerofoils with a serrated trailing edge based on Amiet’s theory. *Journal of Sound and Vibration*, 512:116352, 2021.
- [17] Y. Hu, Z. Wan, C. Ye, D. Sun, and X. Lu. Noise reduction mechanisms for insert-type serrations of the naca-0012 airfoil. *Journal of Fluid Mechanics*, 941:1–34, 2022.
- [18] S. Shubham, R. D. Sandberg, S. Moreau, and H. Wu. Surface pressure spectrum variation with mach number on a cd airfoil. *Journal of Sound and Vibration*, 526:116762, 2022.
- [19] C. Geuzaine and J. F. Remacle. Gmsh: a three-dimensional finite element mesh generator with built-in pre- and post-processing facilities. *International Journal for Numerical Methods in Engineering*, 79(11):1309–1331, 2009.
- [20] H. G. Weller, G. Tabor, H. Jasak, and C. Fureby. A tensorial approach to computational continuum mechanics using object-oriented techniques. *Computers in Physics*, 12(6), 1998.
- [21] K. S. Brentner, G. A. Bres, G. Perez, and H. E. Jones. Maneuvering rotorcraft noise prediction: a new code for a new problem. In *American Helicopter Society Aerodynamics, Acoustics, and Test and Evaluation Technical Specialist Meeting*, San Francisco, CA, Jan 23–25 2002.
- [22] G. A. Brès, K. S. Brentner, G. Perez, and H. E. Jones. Maneuvering rotorcraft noise prediction. *Journal of Sound and Vibration*, 275:719–738, 2004.
- [23] S. Lee, K.S. Brentner, F. Farassat, and P.J Morris. Analytic formulation and numerical implementation of an acoustic pressure gradient prediction. *Journal of Sound and Vibration*, 319(3-5):1200–1221, 2009.
- [24] M. Mancinelli, T. Pagliaroli, T. Di Marco, Camussi. R., T. Castelain, and O. Leon. Hydrodynamic and acoustic wavelet-based separation of the near-field pressure of a compressible jet. In *2016 AIAA/CEAS Aeroacoustics Conference*, Lyon, France, May 30–June 1 2016.
- [25] M. Mancinelli, T. Pagliaroli, T. Di Marco, Camussi. R., and T. Castelain. Wavelet decomposition of hydrodynamic and acoustic pressures in the near field of the jet. *Journal of Fluid Mechanics*, 813:716–749, 2017.
- [26] A. Garcia-Sagrado and T. Hynes. Wall pressure sources near an airfoil trailing edge under turbulent boundary layers. *Journal of Fluids and Structures*, 30:3–34, 2012.
- [27] N. J. Georgiadis, D. P. Rizzetta, and C. Fureby. Large-eddy simulation: current capabilities, recommended practices, and future research. *AIAA Journal*, 48(8):1772–1784, 2010.
- [28] K. S. Brentner and F. Farassat. Modelling aerodynamically generated sound of helicopter rotors. *Progress in Aerospace Sciences*, 39(2-3):83–120, 2003.
- [29] F. Farassat. The prediction of helicopter discrete frequency noise. *Vertica*, 7(4):309–320, 1983.
- [30] R. Camussi and G. Guj. Orthonormal wavelet decomposition of turbulent flows: intermittency and coherent structures. *Journal of Fluid Mechanics*, 348:177–199, 1997.
- [31] J. Ruppert-Felsot, M. Farge, and P. Petitjeans. Wavelet tools to study intermittency: application to vortex bursting. *Journal of Fluid Mechanics*, 636:427–453, 2009.
- [32] D. L. Donoho and J. M. Johnstone. Ideal spatial adaptation by wavelet shrinkage. *Biometrika*, 81(3):425–455, 1994.
- [33] J. N. Kutz, S. L. Brunton, B. W. Brunton, and J. L. Proctor. *Dynamic Mode Decomposition: Data-Driven Modeling of Complex Systems*. Society for Industrial and Applied Mathematics, Philadelphia, PA, 2016.
- [34] P. J. Schmid. Dynamic mode decomposition of numerical and experimental data. *Journal of Fluid*

- Mechanics*, 656:5–28, 2010.
- [35] Thomas F. Brooks, D. S. Pope, and Michael A. Marcolini. Aifoil self-noise and prediction. NASA RP 1218, 1989.
 - [36] S. P. Gravante, A. M. Naguib, C. E. Wark, and H. M. Nagib. Characterization of the pressure fluctuations under a fully developed turbulent boundary layer. *AIAA Journal*, 36(10):1808–1816, 1998.
 - [37] S. Grizzi and R. Camussi. Wavelet analysis of near-field pressure fluctuations generated by a subsonic jet. *Journal of Fluid Mechanics*, 698:93–124, 2012.
 - [38] D.H. Kang and S. Lee. Application of wavelet analysis to trailing-edge noise. In *2022 AIAA/CEAS Aeroacoustics Conference*, Southampton, United Kingdom, June 14–17 2022.